Arch. Metall. Mater. **68** (2023), 2, 531-540

DOI: https://doi.org/10.24425/amm.2023.142432

BIANLI QUAN[1], ZHIPING XIE[2*]

STUDY ON CORROSION BEHAVIOR OF Q235 STEEL AND 16MN STEEL BY ELECTROCHEMICAL AND WEIGHT LOSS METHOD

This study investigates the corrosion characteristics of Q235 steel and 16Mn steel in the sulfur-containing alkaline solution. The composition and the morphology of the corrosion products were analyzed by XPS and SEM respectively. The electrochemical behavior of Q235 steel and 16Mn steel was evaluated by potentiodynamic polarization curve and EIS. The results indicated that the corrosion rate of Q235 steel is greater than 16Mn steel in the early corrosion. Pitting and selective corrosion appeared on the surface of the two steels, and the surface product layer was granular and defective. XPS and EDS indicate that the structurally stable iron oxide is formed on the surface of the two steels. Electrochemical results show the corrosion kinetics of Q235 steel and 16Mn steel are simultaneously controlled by the charge transfer and ion diffusion, and the formation mechanism of corrosion products was clarified.

Keywords: Q235 steel; 16Mn steel; Sulfur; Corrosion mechanism; Alkaline solution

1. Introduction

In recent years, because of the shortage of high-quality bauxite, high-sulfur bauxite alumina with the higher alumina-silica ratio is used in Bayer alumina production, and the sodium aluminate solutions contains a higher concentration of S^{2-} and a small amount of SO_4^{2-}, $S_2O_3^{2-}$, SO_3^{2-}, *etc.* [1]. $S^{2-}$and $S_2O_3^{2-}$ are considered the most aggressive species of Bayer liquor, which will corrode equipment materials [2,3]. With the progress of production, the corrosion of equipment materials by sulfur in different alumina plants will cause significant economic losses [4]. As a traditional pressure vessel material, Q235 steel and 16Mn steel are often used as the materials of dissolution equipment, dilution tank and Bayer mother liquor evaporation equipment. The two steels will suffer severe corrosion if exposed to a sulfur-containing solution for a long time. So, it is very important to study the corrosion of sulfur to the two steels in a sulfur-containing solution.

Because of high sulfur bauxite are mainly distributed in China [5], the corrosion behavior of steel is relatively less studied in the sodium aluminate solution containing S^{2-} and $S_2O_3^{2-}$ [3,6]. Although the corrosion of sulfur on steel in the alkaline solution has been studied by many scholars, most of them mainly focus on the corrosion of steel in white liquor, which contained the highest concentrations of alkaline and sulfur-contained species. Esteves et al. [7] studied the cyclic potentiodynamic polarization behavior of two steels in white and green liquors from a pulp processing plant. Feng, et al.[8] evaluated the effect of temperature on the corrosion behavior of S32750 steel in white liquor. But the alumina production system contains lower concentrations of alkaline and sulfur-contained species. Chen et al. [3] studied the corrosion behavior of 16Mn steel in sulfide-containing Bayer liquid, and the results indicated that S^{2-} anion increase significantly the corrosion rate of the steel and $S_2O_3^{2-}$ anion had no effect on corrosion of the steel. However, there is the interaction between the coexistence of S^{2-} and $S_2O_3^{2-}$ in the solution, which is often referred to the corrosion of steel in the literature [9-11].

The purpose of the study is to evaluate the effect of interaction between the coexistence of S^{2-} and $S_2O_3^{2-}$ on Q235 steel and 16Mn steel corrosion in the alkaline solution. The corrosion rate of Q235 steel and 16Mn steel with different corrosion time was discussed using weight loss method and potentiodynamic polarization curves method. The synergistic effect between S^{2-} and $S_2O_3^{2-}$ will be discussed in detail via scanning electron microscope (SEM), Energy Dispersive Spectrometer (EDS), X-ray photoelectron spectroscopy (XPS) and electrochemical

[1] GUIZHOU UNIVERSITY, COLLEGE OF MATERIALS AND METALLURGY, GUIYANG, 550025, CHINA
[2] GUIZHOU NORMAL UNIVERSITY, SCHOOL OF MECHANICAL & ELECTRICAL ENGINEERING, GUIYANG, 550025, CHINA
* Corresponding author: bianli0901@163.com

measurements. Due to the complex composition of the sodium aluminate solution, the research on the corrosion behavior of the two steels is greatly hindered. So, the study of steel corrosion in the sodium hydroxide system will provide the reference for the corrosion mechanism of steels in the complex sodium aluminate solution and the protection of equipment material.

2. Experiments

2.1. Specimens and Test Solutions

The chemical compositions of Q235 steel and 16Mn steel in this study are shown in TABLE 1. The dimension of Q235 steel and 16Mn steel are 15 mm×15 mm×1.0 mm and 20 mm×10 mm×1.0 mm, respectively. Surface of the specimens was achieved by grinding up to 1800 grit SiC abrasive paper and acetone accompanying with intermediate water rinses respectively. Fig. 1 shows the morphology of two steels before corrosion [12]. It can be seen from Fig. 1 that the surface of Q235 steel is smoother than that of 16Mn steel. Five Q235 steel coupons and five 16Mn steel coupons were employed in each experiment. Three coupons were used to assess the weight change (corrosion rate), while the other two steel sheets were used to analyze the morphology and chemical composition. The marked steel sheets were passivated in 65% concentrated nitric acid solution for 15 minutes.

Experiments were conducted in the corrosion solutions containing 115g·L^{-1} NaOH, 5g·L^{-1} S^{2-} and 4 g·L^{-1} $S_2O_3^{2-}$. The corrosion solutions were prepared by dissolving $Na_2S{\cdot}9H_2O$ and $Na_2S_2O_3{\cdot}5H_2O$ into the alkaline solution. The pH of the solution is 13.75 by laboratory test. All the experiments were conducted at 328K without aeration.

TABLE 1

Chemical composition (Wt %) of Q235 steel and 16Mn steel

Sample	C	Si	Mn	Cr	P	S	Fe
Q235 steel	0.207	0.055	0.233	0.105	0.069	0.019	Bal
16Mn steel	0.178	0.290	1.645	0.041	0.056	0.017	Bal

2.2. The Corrosion Experiment

The corrosion experiments were carried out in the salt spray corrosion chamber (GB/T24195-2009) at 328K [13]. The schematic diagram of salt spray corrosion chamber is shown in Fig. 2. The test solutions were supplemental daily. Before measuring the weight lost, the corrosion products were removed using the chemical products-cleanup method (GB/T 6074-1992) (500mL distilled water + 500 mL HCl + 10 g hexamethylenetetramine). The corrosion rate r (g·m^{-2}·h^{-1}) was measured using weight loss method [14], and the calculation formula is as follows:

$$r = 10^4 \times \frac{W_1 - W_2}{S \times t} \quad (1)$$

where W_1 and W_2 are the quality of the sample before the corrosion (g) and the sample after removal of corrosion products (g), respectively. S is the sample surface area (cm^2), t is corrosion time (h).

2.3. Surface analysis

The morphology and elementary composition of the corrosion products were observed with scanning electron microscopy (SEM) (SUPRA 40) and energy dispersive spectroscopy (EDS) (AZ tec.).

The composition of the corrosion products was tested by means of PHI Quantum 2000 Scanning ESCA Microprobe X-rays photoelectron spectrometer (XPS). Monochroma-tized Al *Ka* radiation (1486.6 eV) was used as the excitation source. After being exposed to the solutions for different concentrations of sulfur, the sample was dried and transferred to the XPS instrument for analysis. The binding energy values were calibrated with reference to the C 1s peak at 284.8 eV. Data processing and Photoelectron peak analytical would be parsed using Multipeak8.0. The narrow scan spectra were fitted with XPS Peak 4.1 software.

SEM morphology was performed on the surface of the steels after the corrosion products were removed. The pit depth was measured by Z-axis non-contact measuring microscope (DMI5000M) with an accuracy of 0.1 um.

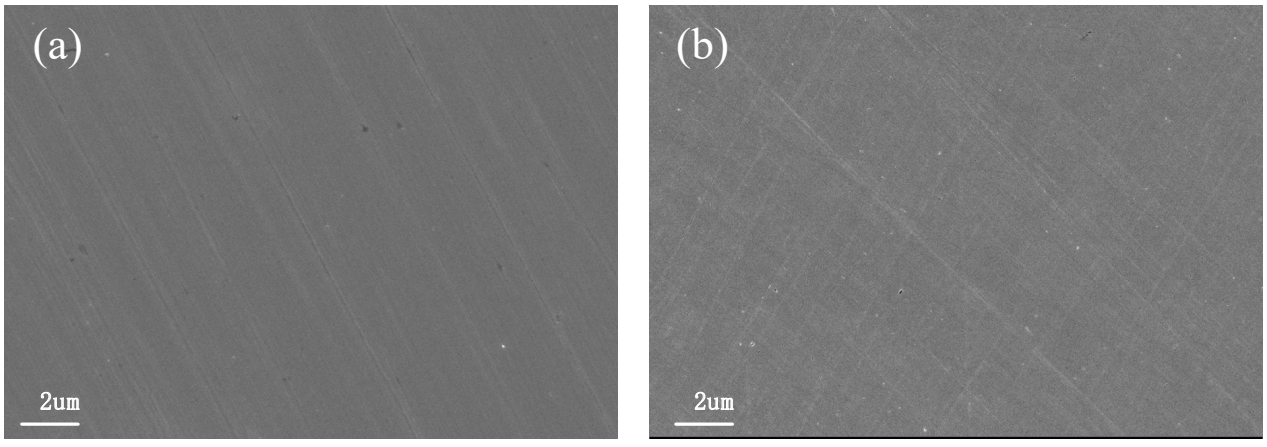

Fig. 1. Morphology of the two steels before corrosion. (a) Q235 steel, (b) 16Mn steel

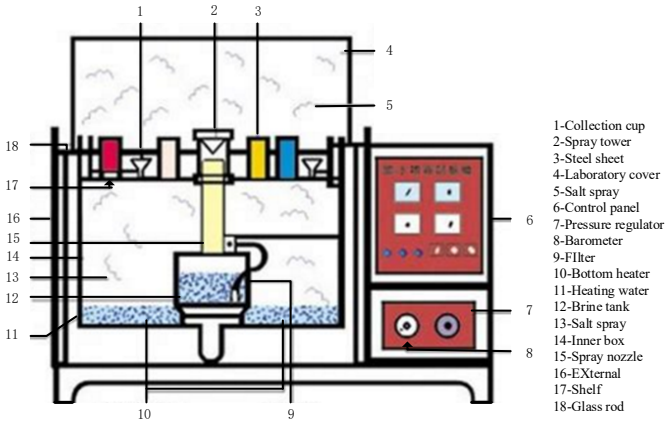

Fig. 2. The schematic diagram of salt spray corrosion experiment

2.4. Electrochemical measurements

Electrochemical experiments were carried out in a conventional three-electrode Polytetrafluoroethylene (PTFE) cell with the counter electrode made of platinum (CE), a saturated calomel electrode (SCE) as reference electrode (RE) and the steel plate studied as the working electrode (WE) with the exposed areas of Q235 steel and 16Mn steel about 2.25 cm^2 and 2 cm^2, respectively. The steel electrodes were immersed in an alkaline solution and placed in a water bath at 328 K in order to obtain the required temperature for the experiment. Potentiodynamic polarization curves measurements were performed at a potential scan rate of $1mV \cdot s^{-1}$ after the stabilization of open-circuit potential (OCP) for 1 h, and the potential range was from –1.50 to 1.0 V vs. open-circuit potential (OCP). EIS measurements were performed at stable OCP in the frequency range from 100 kHz to 10 mHz by 5 points per decade. All potentials reported in this paper were measured with respect to the SCE, which was connected to the cell through a Luggin capillary tip arrangement and a salt bridge to avoid amplification of the electrolyte from constituents of the reference electrode. All the tests were repeated to obtain reproducibility of results. The corrosion data of potentiodynamic polarization curves and EIS were measured and analyzed by a general-purpose electrochemical system (GPES) and a frequency response analyzer (FRA) software.

3. Results and Discussion

3.1. Corrosion Rate

Fig. 3(a) shows the corrosion rate of Q235 steel and 16Mn steel based on weight loss method with different time in the alkaline solutions containing $5g \cdot L^{-1}$ S^{2-} and $4g \cdot L^{-1}$ $S_2O_3^{2-}$. The corrosion rate of two steels decreased with corrosion time. The reason may be that as the corrosion progresses, the resistance to the diffusion of corrosive ions (S^{2-}, $S_2O_3^{2-}$ or OH^-) in the solution to the steel matrix increases. This conclusion is in agreement with the literature [15,16]. The maximum corrosion rate of Q235 steel and 16Mn steel is $243.84\ g \cdot m^{-2} \cdot h^{-1}$ and $113.66\ g \cdot m^{-2} \cdot h^{-1}$, respectively. The corrosion rate of Q235 steel is greater than 16Mn steel in the early corrosion. The reason is that the manganese element of 16Mn steel accelerates the transformation of surface corrosion layer, which makes the surface corrosion easy to form compact FeOOH which has great resistance to the diffusion of ions to the metal surface. This conclusion is different from the literature [12], which may be caused by surface passivation treatment. The other reason for this is Q235 steel in the passivation process reacts more easily with the surface defects formed the oxide layer and accelerated the corrosion rate. These results are also supported by the research result of Wu et al. [17]. Besides, the strong alkaline solution has high concentrations of OH^- which hinder the secondary hydrolysis reaction of sodium sulfide. Therefore, a higher concentration of HS^- is conducive to the formation of sulfide film and reduces the corrosion rate [18].

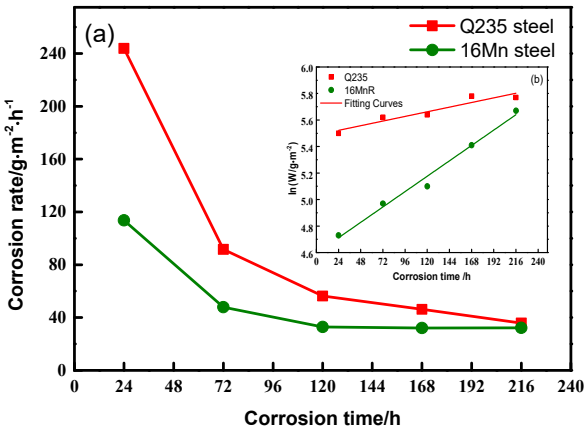

Fig. 3. Corrosion rates of Q235 steel and 16Mn steel by weight loss method. (a) Relationship between corrosion rate and time, (b) Fitting curves

In order to obtain the linearization relationship, the logarithm of W is plotted against time. The results are shown in TABLE 2 and Fig. 3(b). It can be seen that the fitting curves have good agreement with the test result. It can be seen from Fig. 3(b) The experimental results are basically consistent with the accepted logarithmic function of corrosion rate and time, that is:

$$\ln W = a + bt \tag{2}$$

where W is loss of weight per unit area ($g \cdot m^{-2}$), t is corrosion time (h), a and b are constants, which are the intercept and slope of straight line, respectively.

As seen from TABLE 2, the a value of 16Mn steel is smaller than that of Q235 steel, and the b value is larger in the early corrosion. The reason is that the alloy elements have certain influence on the corrosion. The literature [19] found that the corrosion rate of 35CrMn steel was obviously lower than that of Q235 steel. However, according to the fitting results, with the extension of corrosion time, the corrosion rate of 16Mn steel may be higher than that of Q235 steel. It may be that the surface corrosion products of 16Mn steel reacted with ions in the solution, and its composition and structure changed, which led to the acceleration of corrosion in the later stage.

TABLE 2

Intercept and slope obtained from ln(W)-t linear fitting for Q235 steel and 16Mn steel

Sample	*a*	*b*	Coefficient correlation R^2
Q235 steel	5.487	0.0015	0.875
16Mn steel	4.596	0.0048	0.981

3.2. Surface Morphology and Composition

The surface morphology and element distribution of Q235 steel and 16Mn steel for 120 h in the alkaline solution containing $5g \cdot L^{-1}$ S^{2-} and $4g \cdot L^{-1}$ $S_2O_3^{2-}$ are shown in Fig. 4 and TABLE 3. It can be seen that the corrosion products on the surface of the two steels are not uniformly distributed. A large number of granular corrosion products accumulated in the defect, and the corrosion is more serious and sulfur content increase gradually, revealing that the protective ability of the passive film is lost and the surface corrosion is transformed gradually. In addition, the corrosion product layer does not totally cover the steel surface and cannot be considered as a homogeneous layer but rather as a defective layer. The corrosion of two steels preferentially takes place at defect, which view consistent with the analysis before and the literature [6]. The surface of Q235 steel and 16Mn steel is locally covered by the corrosion products. Selective corrosion and pitting corrosion occur on Q235 steel and 16Mn steel surface. The corrosion products of the two steels surface are generally featured with a granular, porous structure, depositing loosely [20]. EDS analysis shows that the corrosion products are mainly composed of three elements (O, S and Fe). The corrosion products generated priority in the defects [21,22] or the scratches [23], which can be seen from the morphology of two steels.

TABLE 3 indicates the element distribution of before corrosion and corrosion products on the two steels surface (Point scanning). It can be seen from TABLE 3 that after nitric acid treatment, the oxygen element on the surface of the steel increases, and the iron element decreases, which may mainly exist in the form of oxides, indicating that nitric acid has a certain degree of influence on the steel surface. The content of sulfur and oxygen element of the corrosion products increases after corrosion, but oxygen content is relatively higher than the matrix after the surface passivation. Herein higher oxygen is partly from the passivation process. The content of manganese decreased for 16Mn steel, which shows that manganese is involved in the chemical reaction and formed MnS. It hinders the corrosion from proceeding. This view is also reported by the literature [15,24]. The reason of the content of sulfur increased is that the electrochemical reaction is faster at first, but the corrosion products plating on steel surface are partly protective of the matrix metal with reaction and increase the reactant diffusion resistance. It can be seen from TABLE 3 that the atomic ratio of corrosion product layer is Fe: S = 1:2, Fe: O = 3:4 for Q235 steel, and the atomic ratio of corrosion product layer is Fe: S = 1:2, Fe: O = 1:2 for 16Mn steel [25]. Therefore, it can be inferred that the surface

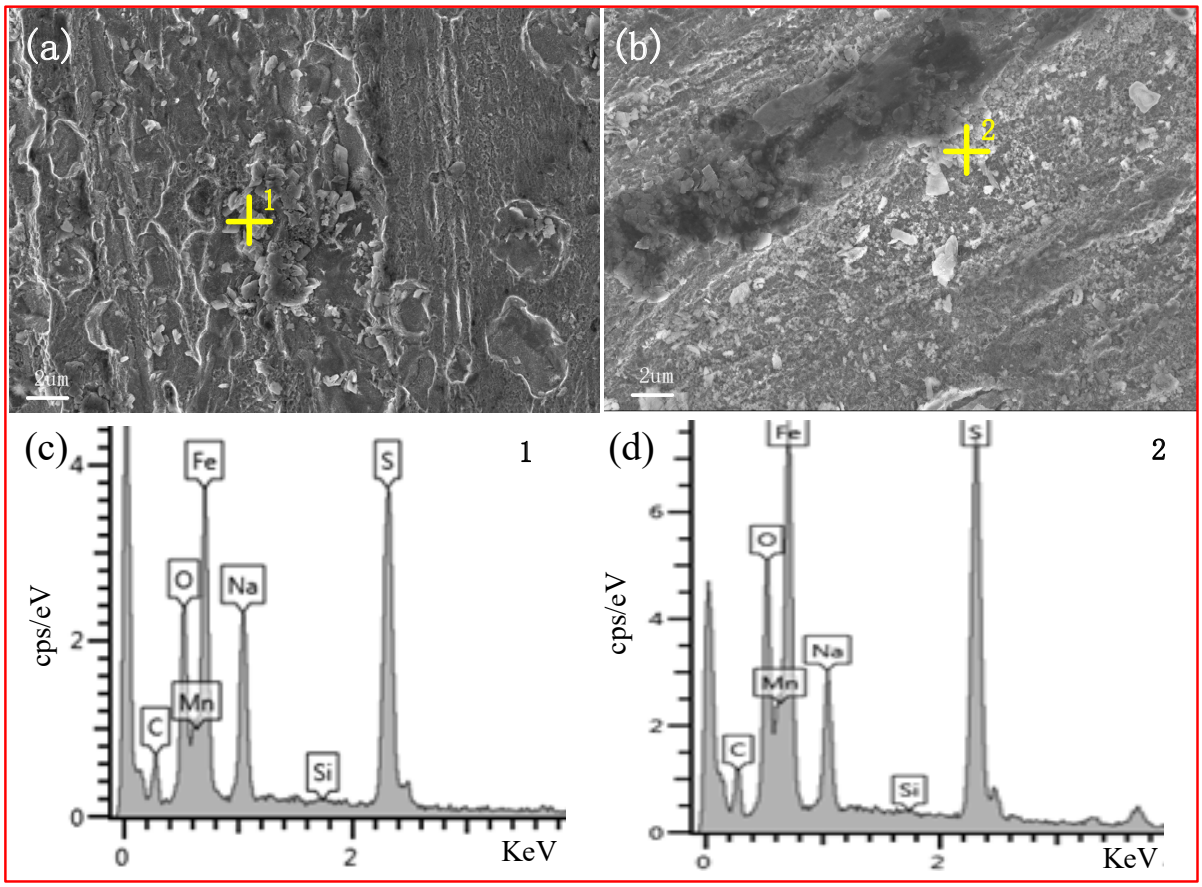

Fig. 4. The morphology and element composition of the corrosion products on Q235 steel surface (a, c) and 16Mn steel surface (b, d)

corrosion of Q235 steel is mainly composed of Fe_3O_4 and FeS_2, while the surface corrosion of 16Mn steel is mainly composed of FeOOH and FeS_2.

TABLE 3

The elements distribution of before corrosion (Wt.%) and corrosion products on two steels surface (Wt.% and At.%)

Elements		C	O	S	Na	Si	Mn	Fe
Wt.% (Before corrosion)	Q235 steel	2.74	1.39	0.00	0.13	0.18	0.00	95.57
	16Mn steel	3.36	1.15	0.00	0.19	0.38	2.47	92.46
Wt.% (After corrosion)	Q235 steel	9.08	10.32	22.32	10.03	0.17	0.40	47.68
	16Mn steel	9.90	12.00	24.28	6.35	0.13	0.10	47.34
At.% (After corrosion)	Q235 steel	22.23	18.97	20.47	12.83	0.18	0.21	25.11
	16Mn steel	23.83	21.67	21.93	7.97	0.13	0.05	24.41

Fig. 5 shows the surface morphologies of two steels after removing corrosion products. The matrix metal shows a rough etched surface texture, and the surface of two steels is greatly corroded. As seen from Fig. 5, pitting corrosion occurs at the surface defects of the two steels, and the formed pits are irregular. Meanwhile, in addition to pitting corrosion, a large number of corrosion scratches also appeared on the steels surface, the cause of which was surface defects.

In order to measure a pit depth and calculate localized corrosion rate, Difference of Microscope Focus (DMF) analysis was performed for all samples [26]. Table 4 lists the corrosion rates obtained from weight loss method and DMF analysis. Basing on the data of weight loss method, the corrosion rate of Q235 steel is larger than that of 16Mn steel from, but the corrosion rates of two steels are similar based on the maximum pit depth of DMF. A similar finding has been reported in the literature [16]. The corrosion of Q235 steel is relatively serious from the numerical point of view.

TABLE 4

Comparison of corrosion rates obtained from weight loss method and DMF Analysis

Steel sample	Weight loss method ($g \cdot m^{-2} \cdot h^{-1}$)	Maximum pit depth from DMF (μm)	Pit penetration rate (mm/a)
Q235 steel	91.64	7.7	0.937
16Mn steel	47.89	7.6	0.925

3.3. XPS of Surface Corrosion Products

Fig. 6 shows the decomposition of peaks for Fe2p, S2p and O1s of the corrosion products formed on Q235 steel and 16Mn steel for 120 hours. Peak decomposition of Fe2p, S2p and O1s core level spectra are in agreement with the published results [27,28]. Fe2p, S2p, O1s spectrum can be curve-fitted

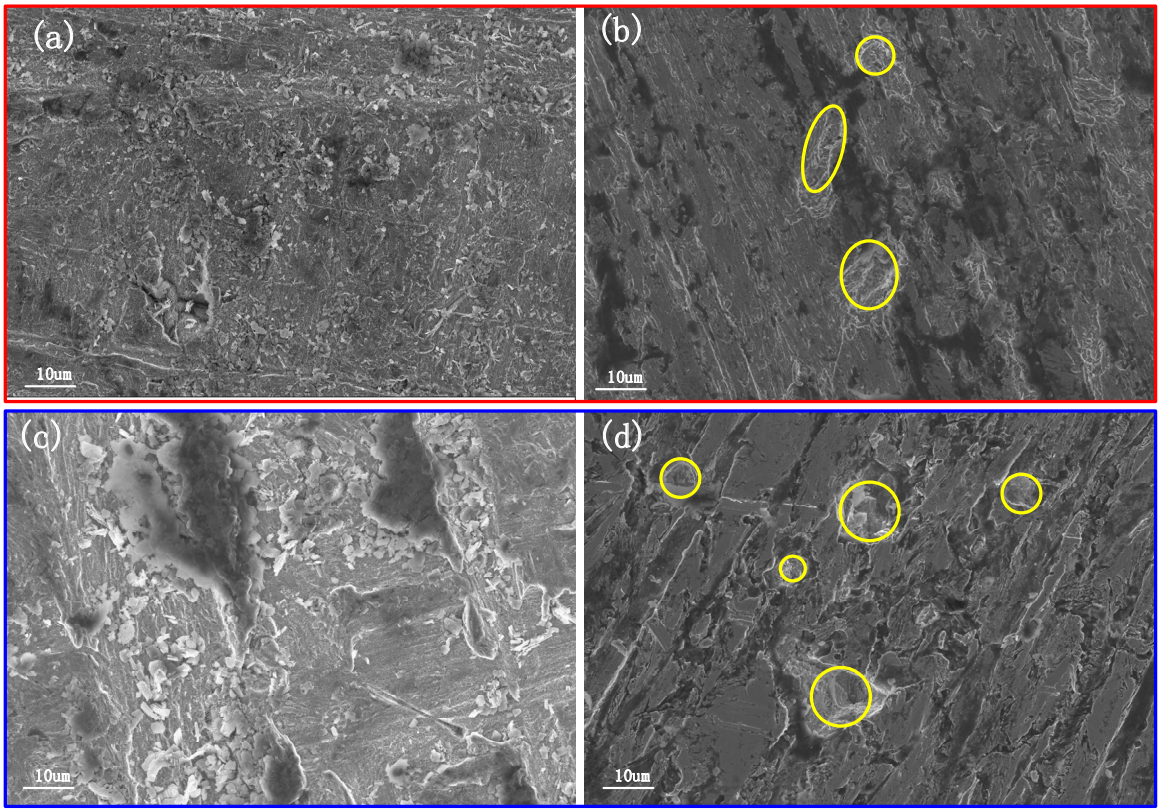

Fig. 5. SEM morphologies of steel surface. (a) Q235 steel; (b) Q235 steel surface to remove surface corrosion products; (c) 16Mn steel; (d) 16Mn steel surface to remove surface corrosion products

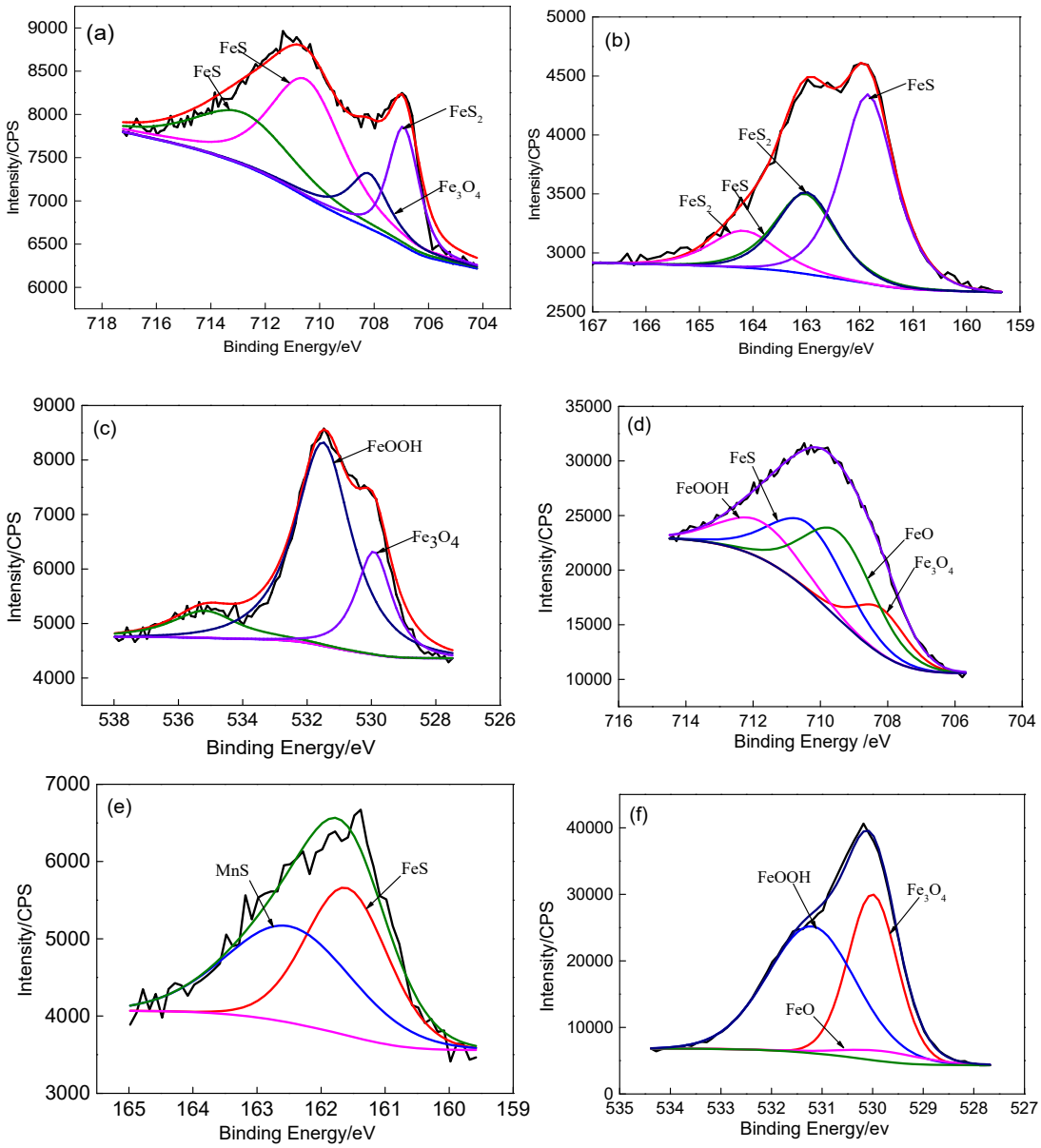

Fig. 6. XPS patterns of the corrosion products on two steels surface. Fe 2p (a), S2p (b) and O1s(c) of Q235 steel; Fe 2p (d), S2p (e) and O1s (f) of 16Mn steel

and indicates that the surface corrosion products of Q235 steel are mainly composed of FeS, FeS_2, Fe_3O_4 and FeOOH. This conclusion has been reported in literature [10].

Fe2p spectrum can be curve-fitted with four peaks for 16Mn steel (Fig. 6e). The peaks at 708.2 eV, 709.4 eV, 710.3 eV and 711.8 eV correspond to Fe_3O_4, FeO, FeS and FeOOH, respectively. In O1s spectrum of 16Mn steel (Fig. 6f), a broad peak and two narrow peaks are observed at about 528-534 eV in the solutions. O1s spectrum can be curve-fitted with three peaks. The peak at 529.8 eV, 530.0eV and 531.2 eV is attributed to O^{2-}, Fe_3O_4 and FeOOH in oxides, respectively. S2p spectrum can be curve-fitted with two peaks for 16Mn steel (Fig. 6g). The peaks at 161.6 eV and 162.5 eV correspond to FeS and MnS, respectively. Fig. 6(e-g) indicates that the surface corrosion products of 16Mn steel are mainly composed of FeS, MnS, FeO, Fe_3O_4 and FeOOH. The formation of a stable corrosion layer can inhibit the diffusion of corrosive species, which will be beneficial to improve the corrosion resistance.

Fig. 7 is E-pH diagram of Fe-S-H_2O at 328K, derived from a chemical equilibrium and reaction software database [29]. E-pH diagram shows the thermodynamically phases may exist in Fe-S-H_2O systems under the given experimental conditions. The solid oxide formations of Fe_2O_3 and Fe_3O_4 and soluble anion compounds $HFeO_2$(-a) is expected in the pH range tested. Fig. 7 indicates that the stable phase of the steel surface can be a Fe_2O_3 or Fe_3O_4 film in pH of 14. If an insoluble film is stable, the corrosion process will be suppressed, and the corrosion rate will slow down and depend on the stability and electronic conductivity properties of the passive film. As showed in Fig. 7, the formation of FeS and FeS_2 is thermodynamically favorable in pH of 14. Similarly, the work by Tromans [30] has shown that sulfur is incorporated into Fe_3O_4 film in the region of critical

current density, below the active-passive transition region of potentiodynamic polarization curve. Similar results were found in this study.

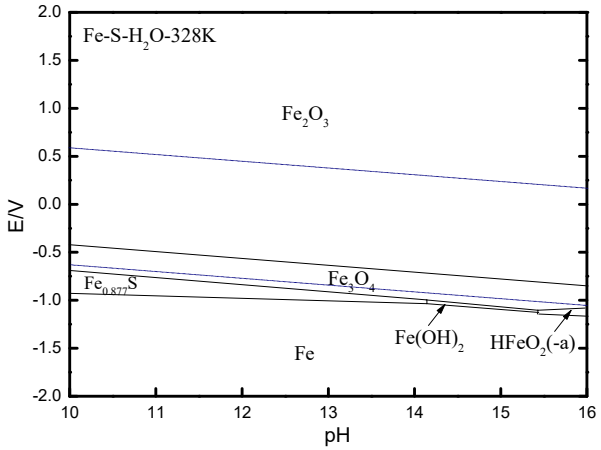

Fig. 7. E-pH diagram of Fe-S-H_2O at 328K

3.4. Potentiodynamic Polarization Curves

Fig. 8 is the potentiodynamic polarization curves of Q235 steel and 16Mn steel in the alkaline solutions containing 5g·L^{-1} S^{2-} and 4g·L^{-1} $S_2O_3^{2-}$. As can be seen from Fig. 8, the anode process shows the phenomenon of activation-transition-passivation, which indicate that the dissolution of iron and the transformation of iron compounds occur on the anode, and a compact corrosion products film is formed on the surface. It can be seen from the potentiodynamic polarization curves that the two steels have the same cathodic reaction and different anodic reactions. This could be due to the fact that the corrosion process involved the transformation of corrosion products, always maintaining the surface active [31]. The corrosion potential (E_{corr}) of Q235 steel and 16Mn steel is nearly –1.20 V vs. SCE in the active state. At the potentials –0.9 V vs. SCE, the curves

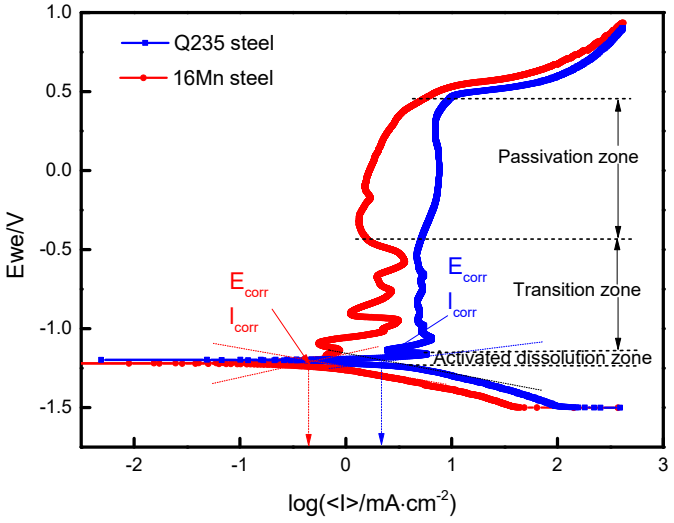

Fig. 8. Potentiodynamic polarization curves of Q235 steel and 16Mn steel

exhibit a humped shape, corresponding to two reactions. One is the dissolution of the exposed steel anode into the electrolyte as $Fe(OH)_3^-/HFeO_2$(-a), and the other is the oxidation of $S_2O_3^{2-}$ to higher forms, as described by Zou [32].

The determination of corrosion parameters (E_{corr} and I_{corr}) could provide more information about the overall corrosion process. TABLE 5 shows the corrosion potentials (E_{corr}) and corrosion currents (I_{corr}) of two steels obtained from Tafel fitting of the potentiodynamic polarization curves. Generally speaking, a higher current density corresponds to a higher corrosion rate. So, the corrosion rate of Q235 steel is greater than that of 16Mn steel. It is consistent with the results of weight loss analysis.

TABLE 5

Electrochemical parameters fitted from potentiodynamic polarization curves

Sample	E_{corr}/V	I_{corr}/ uA·cm^{-2}	β_a/mV	β_c/mV	R_p/ W·cm^2	R^2
Q235 steel	–1.20	1497.10	50.2	136.7	9.13	0.948
16Mn steel	–1.22	511.68	318.6	136.2	44.30	0.999

3.5. Electrochemical impedance spectroscopy

Fig. 9 is EIS of Q235 steel and 16Mn steel in the alkaline solutions containing 5g·L^{-1} S^{2-} and 4g·L^{-1} $S_2O_3^{2-}$. Nyquist plots of Q235 steel and 16Mn steel contain two capacitance-resistance arcs and a Warburg diffusion, which show that the diffusion resistance of ions to the metal surface is larger. That is to say, the impedance caused by the concentration polarization in the corrosion process could not be ignored, the corrosion kinetics of Q235 steel and 16Mn steel are consistent. Capacitance-resistance arc of 16Mn steel is flatter than that of Q235 steel, indicating that the dispersion effect of the corrosion layer on 16Mn steel surface is stronger. Bode plots show that the electrode process of Q235 steel and 16Mn steel contains two time constants (τ_{ct} and τ_f) is the charge transfer of intermediate frequency response and surface film layer of high frequency response respectively, and the Warburg impedance caused by ion diffusion (Z_w).

Based on the above analysis, EIS fitting of Fig. 9 was carried out by using the equivalent circuit of Fig. 10 by means of Zview software. The similar equivalent circuit has been proposed by other researches [33-34]. Electrochemical parameters are shown in TABLE 5. In the equivalent circuit, R_s is solution resistance, R_f and Q_f (CPE1) are the corrosion layer resistance and capacitance respectively, R_{ct} and Q_{dl} (CPE2) are charge transfer resistance and double layer capacitance respectively, and Z_W represents the Warburg diffusion of ions. R_{ct} of 16Mn steel is larger than Q235 steel in TABLE 5, indicating that the charge transfer resistance of 16Mn steel is larger when corrosion occurs. n_{dl} value of 16Mn steel is less than Q235 steel, indicating that the surface is more uneven. R_f of the two steels are approximately equal, indicating that the corrosion product layers formed on the surfaces of the two steels have similar characteristics. It can be seen that the difference between R_f and R_{ct} of the two steels is not very

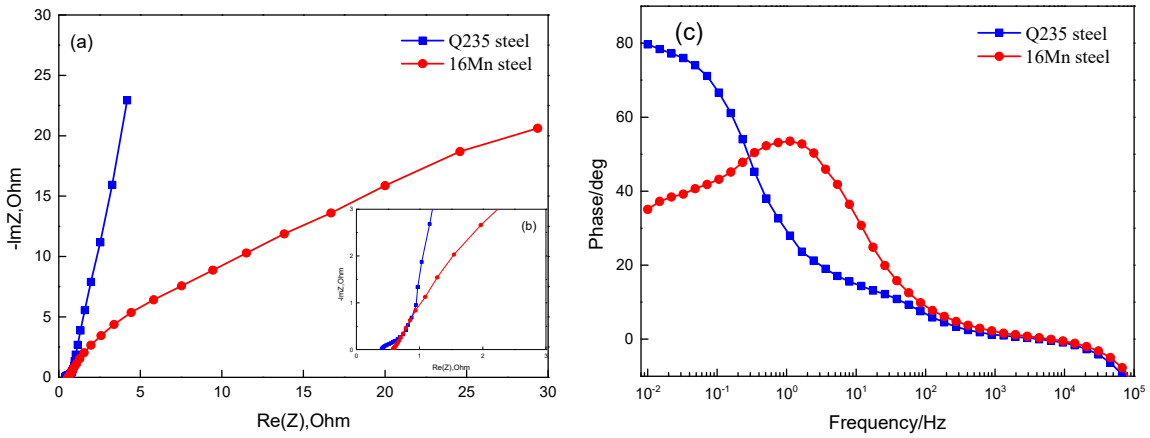

Fig. 9. EIS of Q235 steel and 16Mn steel. Nyquist plots (a, b), Bold plots (c)

significant, which suggests that corrosion kinetics are controlled by the charge transfer and ion diffusion. This result is consistent with potentiodynamic polarization curves and morphologies analysis.

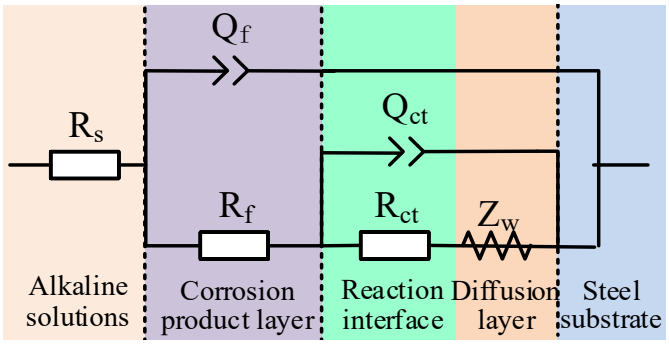

Fig. 10. Equivalent circuit for EIS of Q235 steel and 16Mn steel

4. Corrosion Mechanisms

In order to analyze the effect of sulfur on the corrosion behavior of Q235 steel and 16Mn steel in the alkaline solution containing sulfur in detail and in depth, the formation mechanism of corrosion products and the corrosion mechanism were discussed based on SEM, EDS, XPS, electrochemistry analysis and literature [2,21].

In the sulfur-containing alkaline solution, the main form of sulfide is HS^-. Compared with hydrogen ion and hydroxyl ions, HS^- as an intermediate is much easier adsorbed on the electrode. So, the overall anodic dissolution reaction may be written as reactions (3-6). Among them, reaction (3) corresponds to the anodic activation, and reactions (4-6) correspond to the anodic transition zone shown in Fig. 8.

$$Fe + 2H_2O = HFeO_2^- + 3H^+ + 2e \quad (3)$$

$$HFeO_2^- + S^{2-} + 3H^+ = FeS + 2H_2O \quad (4)$$

$$FeS + HS^- = FeS_2 + H^+ + 2e \quad (5)$$

$$2FeOOH + S_2O_3^{2-} + 12H^+ + 10e = 2FeS + 7H_2O \quad (6)$$

Herein thiosulfate acted as the principal cathodic depolarization in the electrochemical reaction [22]. The reaction of S^{2-} and $S_2O_3^{2-}$ is shown in reaction (7):

$$2S^{2-} + S_2O_3^{2-} + 6OH^- = S_2^{2-} + 2SO_3^{2-} + 3H_2O + 6e \quad (7)$$

Reaction 7 is a reaction of losing electrons, which has a certain influence on the electron loss reaction of the anode. So, anodic dissolution of steel was inhibited. The corrosion rate is reduced, which is very close to the result of the weight loss method.

Meanwhile, S_2^{2-}, $S_2O_3^{2-}$ and OH^- may compete for electrons at the cathode. So, an electronic reaction may occur at the cathode as shown in Reactions (8-11):

$$O_2 + 2H_2O + 4e = 4OH^- \quad \varphi^{\theta}_{O_2/OH^-} = -0.401V \quad (8)$$

$$S_2^{2-} + 2e = 2S^{2-} \quad \varphi^{\theta}_{S_2^{2-}/S^{2-}} = -0.51V \quad (9)$$

$$2SO_3^{2-} + 3H_2O + 4e = S_2O_3^{2-} + 6OH^- \quad \varphi^{\theta}_{SO_3^{2-}/S_2O_3^{2-}} = -0.58V \quad (10)$$

$$SO_3^{2-} + 3H_2O + 6e = S^{2-} + 6OH^- \quad \varphi^{\theta}_{SO_3^{2-}/S^{2-}} = -0.61V \quad (11)$$

TABLE 6

EIS fitting results of Q235 steel and 16Mn steel

Steel	R_s ($\Omega\cdot cm^2$)	R_f ($\Omega\cdot cm^2$)	CPE_f ($\Omega^{-1}\cdot cm^{-2}\cdot s^{-n}$)	n_f	R_{ct} ($\Omega\cdot cm^2$)	CPE_{dl} ($\Omega^{-1}\cdot cm^{-2}\cdot s^{-n}$)	n_{dl}	W_R ($\Omega\cdot cm^2$)	W_T	W_P	R^2
Q235	0.40	0.34	0.09	0.79	1e-7	0.11	0.98	1.44	0.43	0.46	2e-4
16Mn	0.58	0.27	0.02	0.85	8.02	0.03	0.82	0.83	1e-3	0.20	2e-4

According to the priority order of the electron reduction reaction at the cathode, the higher the potential, the reduction reaction occurs preferentially at the cathode. When it comes to gas, it must consider over-potential, so, in contrast to reaction (9), (10) and (11), reaction (8) will not occur. As plain alkaline solution, reaction 8 will occur at the anode. Therefore, the cathode reaction may proceed according to the reactions (9), (10) and (11), and their Nernst equations are shown in Equations (12), (13) and (14).

$$\varphi_{S_2^{2-}/S^{2-}} = \varphi^{\theta}_{S_2^{2-}/S^{2-}} + \frac{2.303RT}{2F}\lg\frac{a_{s_2^{2-}}}{a^2_{s^{2-}}} = -0.51V \quad (12)$$

$$\varphi_{SO_3^{2-}/S_2O_3^{2-}} = \varphi^{\theta}_{SO_3^{2-}/S_2O_3^{2-}} + \frac{2.303RT}{4F}\lg\frac{a^2_{SO_3^{2-}}}{a_{S_2O_3^{2-}}\cdot a^6_{OH^-}} = = 0.787 - 0.0976\,pH = -0.56V \quad (13)$$

$$\varphi_{SO_3^{2-}/S^{2-}} = \varphi^{\theta}_{SO_3^{2-}/S^{2-}} + \frac{2.303RT}{6F}\lg\frac{a_{SO_3^{2-}}}{a_{S^{2-}}\cdot a^6_{OH^-}} = = 0.3 - 0.065\,pH = -0.59V \quad (14)$$

Herein assume that the $a_{S^{2-}}$, $a_{S_2O_3^{2-}}$, $a_{S_2^{2-}}$ and $a_{SO_3^{2-}}$ are 1 in Equations (12), (13) and (14). Thus

$$\varphi_{S_2^{2-}/S^{2-}} > \varphi_{SO_3^{2-}/S_2O_3^{2-}} > \varphi_{SO_3^{2-}/S^{2-}} \quad (15)$$

The cathode reaction preferentially carried out as for reaction (9). But, reactions (10) and (11) would occur later. As can be seen from reactions (9), (10) and (11), S_2^{2-} produced by reaction (7) plays a role of cathode depolarization. So, the corrosion reactions are carrying constantly.

Therefore, the surface corrosion products may generate according to the following reaction at the anode.

$$Fe + 2S^{2-} + 4e = FeS_2 \quad \varphi^{\theta}_{Fe/FeS_2} = -0.189V \quad (16)$$

$$Fe + S^{2-} + 2e = FeS \quad \varphi^{\theta}_{Fe/FeS} = -0.792V \quad (17)$$

According to the oxidation reaction sequence of the anode, the lower the potential, the oxidation reaction occurs preferentially at the anode. Initially, anodic reaction carried out in accordance with reaction (17), the surface corrosion product is FeS. Because there is not enough oxygen in the solution, there is a large amount of S^{2-} in the solution. FeS of corrosion product reacts with S^{2-} in the solution to form FeS_2, as shown in reaction (18).

$$FeS + S^{2-} = FeS_2 + 2e \quad (18)$$

In addition, FeS_2 forms galvanic corrosion with iron substrate, further accelerated corrosion with the increase of corrosion time. The surface corrosion film is damaged, accelerating the dissolution of the anode. As the reaction progresses, unstable sulfide oxidizes into stable oxide. Reactions (19) and (20) correspond to the anodic passivation region in Fig. 7. Due to the formation of iron oxide, the anode is gradually passivated and corrosion becomes slower.

$$3HFeO_2^- + H^+ = Fe_3O_4 + 2H_2O + 2e \quad (19)$$

$$3FeS_2 + 4H_2O + 4e = Fe_3O_4 + 6HS^- + 2H^+ \quad (20)$$

5. Conclusions

In the present paper, the corrosion behavior of Q235 steel and 16Mn steel in the sulfur-containing alkaline solution was studied by the weight loss method and electrochemical methods using SEM, XPS and EDS detection technology. The following main conclusions can be drawn from the results:

(1) Weight loss method showed that the corrosion rate of Q235 steel is greater than that of 16Mn steel. A large number of granular corrosion products accumulated in the defects or the scratches. Pitting corrosion occurs at the surface defects of two steels, and the formed pits are irregular.

(2) Known from the analysis of EDS and XPS, the corrosion products of Q235 steel are mainly composed of FeS, FeS_2, Fe_3O_4 and FeOOH, while that of 16Mn steel are FeS, MnS, FeO, Fe_3O_4 and FeOOH.

(3) Electrochemical results show that the current density of Q235 steel is higher than that of 16Mn steel, and the corrosion kinetics of two steels are simultaneously controlled by the charge transfer and ion diffusion.

(4) The corrosion mechanism is analyzed and the corrosion dynamic model has been established. The cathodic depolarization between S^{2-} and $S_2O_3^{2-}$ has a certain inhibitory effect on the anodic dissolution of steel, S^{2-} and $S_2O_3^{2-}$ participate in the anode reaction and have a certain influence on the composition and morphology of the surface corrosion products. Modeling technology based on the next step is to learn more about steel corrosion process, which establishes a theoretical basis for material selection and protection.

Acknowledgments

This work was supported by Introduction Talent Fund Project of Guizhou University ([2019]43), Major Science and Technology Projects of Guizhou ([2019]3003) and Natural Science Foundation of Guizhou ([2019]1233).

REFERENCES

[1] Z.W. Liu, H.W. Yan, W.H. Ma, Miner. Eng. **149** (8), 106237 (2020). DOI: https://doi.org/10.1016/j.mineng.2020.106237

[2] A. Bhattacharya, P.M. Singh, Corros. Sci. **53**, 71-81 (2011). DOI: https://doi.org/10.1016/j.corsci.2010.09.024

[3] Q.L. Xie, W.M. Chen, Corros. Sci. **86**, 252-260 (2014). DOI: https://doi.org/10.1016/j.corsci.2014.05.019

[4] X.B. Li, F. Niu, G.H. Liu, T.G. Qi, Q.S. Zhou, Z.H. Peng, Trans. Nonferrous Met. Soc. China. **27** (4), 908-916(2017). DOI: https://doi.org/10.1016/S1003-6326(17)60105-5

[5] Z.W. Liu, H.W. Yan, W.H. Ma, P. Xiong, Mining Metall. Explor. **37** (5), 1617-1626 (2020). DOI: https://doi.org/10.1007/s42461-020-00225-6

[6] B.L. Quan, J.Q. Li, C.Y. Chen, Mater. Res. Express. **6** (2), 025607 (2019). DOI: https://doi.org/10.1088/2053-1591/aaf0d8

[7] L. Esteves, M.M.A.M. Schvartzman, W.R.D. Campos, V.F.C. Lins, Corrosion **74** (5), 543-550 (2018). DOI: https://doi.org/10.5006/2558

[8] H. Feng, H.B. Li, S.C. Zhang, Q. Wang, Z.H. Jiang, G.P. Li, Int. J. Electrochem. Sci. (China) **10** (5), 4116-4128 (2015).

[9] L. Stockman, S. Ven. Papperstidn. **63** (13), 425 (1960).

[10] B.L. Quan, J.Q. Li, C.Y. Chen, Int. J. Corrosion **1-6**, 8549312 (2016). DOI: https://doi.org/10.1155/2016/8549312

[11] Q.L. Xie, W.M. Chen, Q. Yang, Corrosion **70** (8), 842-849 (2014). DOI: https://doi.org/10.5006/1206

[12] B.L. Quan, J.Q. Li, C.Y. Chen. Mater. Res. Express. **7** (3), 03560 2(2020). DOI: https://doi.org/10.1088/2053-1591/ab7d57

[13] Y. Nie, J.K. Huang, S.Y. Ma, Z.C. Li, Y.K. Shi, X.F. Yang, Applied Surface Science **527** (10), 146915 (2020). DOI: https://doi.org/10.1016/j.apsusc.2020.146915

[14] L. Kucharikova, T. Liptakova, E. Tillova, M. Bonek, D. Medvecka, Arch. Metall. Mater. **65** (4), 1455-1462 (2020). DOI: https://doi.org/10.24425/amm.2020.133713

[15] Y.S. Choi, F. Farelas, S. Nesic, A.A.O. Magalhaes, Corrosion **70** (1), 38-47 (2014). DOI: https://doi.org/10.5006/1019

[16] A. Fragiel, S. Serna, J. Malo-Tamayo, P. Silva, B. Campillo, E. Martinez-Martinez, Eng. Failure Anal. **105**, 1055-1068 (2019). DOI: https://doi.org/10.1016/j.engfailanal.2019.06.028

[17] Y.H. Wu, T.M. Liu, C. Sun, J. Xu, C.K. Yu, Corros. Eng. Sci. Techn. **45** (2), 136-141(2010). DOI: https://doi.org/10.1179/147842209X12559428167643

[18] H.Z. Cao, J.Y. Zhang, G.Q. Zheng, J.G. Yuan, Corrosion & Protection (China), **23** (10), 427-429 (2002).

[19] X.L. Zuo, B. Xiang, X. Li, Z.D. Wei, J. Mater. Eng. Perform. **21** (4), 524-529 (2012). DOI: https://doi.org/10.1007/s11665-011-9931-2

[20] X. Su, Z.X. Yin, Y.F. Cheng, J. Mater. Eng. Perform. **22** (2), 498-504 (2013). DOI: https://doi.org/10.1007/s11665-012-0291-3

[21] S.S. Xin, M.C. Li, Corros. Sci. **81**, 96-101 (2014). DOI: https://doi.org/10.1016/j.corsci.2013.12.004

[22] R.K. Chasse, P.M. Singh, Metall. Mater. Trans. A. **44** (11), 5039-5053 (2013). DOI: https://doi.org/10.1007/s11661-013-1878-5

[23] D. Siche, D. Klimm, T. Holzel, A. Wohlfart, Journal of Crystal Growth **270** (1-2), 1-6 (2004). DOI: https://doi.org/10.1016/j.jcrysgro.2004.05.098

[24] G.C. Liu, J.H. Dong, E.H. Han, K.E. Wei, Corros. Eng. Sci. Technol. (China) **20** (4), 235-238 (2008).

[25] D. H. Keum, S. Cho, J. H. Kim, et al. Nature Physics **11** (6), 482-486 (2015). DOI: https://doi.org/10.1038/NPHYS3314

[26] X.D. Bai, Q.L. Qiu, P.F. Sun, D.W. Gan, G. Jiang, Atomic Energy Science and Technology (China) **31** (3), 242-245 (1997).

[27] J.B. Tan, X.Q. Wu, E.H. Han, X.Q. Liu, X.L. Xu, H.T. Sun, Corros. Sci. **102**, 394-404 (2016). DOI: https://doi.org/10.1016/j.corsci.2015.10.032

[28] T. Sonmez, M.F. Jadidi, K. Kazmanli, O. Birer, M. Urgen, Vacuum **129**, 63-73 (2016). DOI: https://doi.org/10.1016/j.vacuum.2016.04.014

[29] S. Lee, M.J. Kim, N. Choi, S.Y. Hwang, S.W. Chung, S.J. Lee, Y. Yun, Arch. Metall. Mater. **65** (2), 869-78 (2020). DOI: https://doi.org/10.24425/amm.2020.132833

[30] R. Sriram, D. Tromans, Corros. Sci. **25** (2), 79-91 (1985). DOI: https://doi.org/10.1016/0010-938X(85)90099-X

[31] M.A. Veloz, I. González, Electrochim. Acta. **48** (2), 135-144 (2002). DOI: https://doi.org/10.1016/S0013-4686(02)00549-2

[32] J.Y. Zou, D.T. Chin, Corros. Sci. **33** (4), 477-485 (1988). DOI: https://doi.org/10.1016/0013-4686(88)80164-6

[33] J. Shi, J. Ming, W. Sun et al., Construction and Building Materials **149**, 315-26 (2017). DOI: https://doi.org/10.1016/j.conbuildmat.2017.05.092

[34] S. K. Tang, Z. X. Dai, G. L. Tan et al., Mater. Chem. Phys. **252** (2020). DOI: https://doi.org/10.1016/j.matchemphys.2020.123177